# Photodissociation of the $CH_3O$ and $CH_3S$ radical molecules: An ab initio electronic structure study

A. Bouallagui[a,b], A. Zanchet[a], O. Yazidi[b], N. Jaïdane[b], L. Bañares[c], M.L. Senent[d], and A. García-Vela[a,*]

[a]Instituto de Física Fundamental, Consejo Superior de Investigaciones Científicas, Serrano 123, 28006 Madrid, Spain

[b]Laboratoire de Spectroscopie Atomique, Moléculaire et Applications-LSAMA LR01ES09, Faculté des Sciences de Tunis, Université de Tunis El Manar, 2092, Tunis, Tunisie

[c]Departamento de Química y Física Teóricas, Instituto de Estructura de la Materia, Consejo Superior de Investigaciones Científicas, Serrano 121, Madrid 28006, Spain

[d]Departamento de Química Física, Facultad de Ciencias Químicas (Unidad Asociada I+D+i al CSIC), Universidad Complutense de Madrid, 28040 Madrid, Spain

## Abstract

The electronic states and the spin-orbit couplings between them involved in the photodissociation process of the radical molecules $CH_3X$, $CH_3X \rightarrow CH_3 + X (X = O, S)$, taking place after the $\tilde{A}(^2A_1) \leftarrow \tilde{X}(^2E)$ transition, have been investigated using highly correlated *ab initio* techniques. A two-dimensional representation of both the potential-energy surfaces (PESs) and the couplings is generated. This description includes the C-X dissociative mode and the $CH_3$ umbrella mode. Spin-orbit effects are found to play a relevant role on the shape of the excited state potential-energy surfaces, particularly in the $CH_3S$ case where the spin-orbit couplings are more than twice more intense than in $CH_3O$. The potential surfaces and couplings reported here for the present set of electronic states allow for the first complete description of the above photodissociation process. The different photodissociation mechanisms are analyzed and discussed in the light of the results obtained.

*Corresponding author

E-mail: garciavela@iff.csic.es

## 1. Introduction

The $CH_3O$ and $CH_3S$ radicals of the methoxy family are important intermediates in combustion and atmospheric chemistry.[1–8] The methoxy radical $CH_3O$ is an intermediate in the oxidation chemistry of hydrocarbons like methane, which is important to the ozone budget. In turn, the methylthio radical $CH_3S$ is an internediate in the atmospheric oxidation of organic sulfides of the type $CH_3SCH_3$, $CH_3SSCH_3$, and $CH_3SH$ by OH and $NO_3$.[9–12] Those processes contribute to a relevant portion of the acid precipitation in the atmosphere.

Due to their atmospheric relevance, the spectroscopy and photofragmentation dynamics of the $CH_3O$[13–20] and $CH_3S$[21–31] radicals have been investigated by several authors in the last four decades. Photodissociation of $CH_3X$ (X=O, S) takes place following excitation of the $\tilde{A}(^2A_1) \leftarrow \tilde{X}(^2E)$ transition. In the case of $CH_3O$ three product channels have been identified experimentally[17,18]:

$$CH_3O \rightarrow CH_3 + O, \tag{1}$$

$$CH_3O \rightarrow CH_2 + OH, \tag{2}$$

$$CH_3O \rightarrow CH_2O + H, \tag{3}$$

being (1) the dominant channel, which takes place through a predissociation mechanism. The branching ratio found experimentally for channels (1) and (2) was 3:1,[17] and the probability of channel (3) is significantly smaller. While channel (1) could be considered a possible way to produce $CH_3$ radicals, it is noted that further predissociation of the $CH_3$ product may subsequently occur, which has recently been studied.[32–34] For $CH_3S$ only the $CH_3S \rightarrow CH_3 + S$ channel has been directly observed at the excitation energies investigated,[30,31] although occurrence of the $CH_3S \rightarrow CH_2S + H$ channel has also been proposed based on indirect evidence.[31] Thus, channel (1) is the major photofragmentation channel for both $CH_3O$ and $CH_3S$

radicals.

An interesting aspect of $CH_3O$ and $CH_3S$ is that their $\tilde{X}(^2E)$ state is Jahn-Teller distorted, and all the three nontotally symmetric (of e symmetry) vibrations ($\nu_4$, $\nu_5$, and $\nu_6$) are active in the $\tilde{A}(^2A_1)$ state, thus making possible Jahn-Teller activity upon the $\tilde{A}(^2A_1) \leftarrow \tilde{X}(^2E)$ transition. In the case of channel (1) for $CH_3O$, photodissociation experiments[17,18] found two vibrational progressions (each of them split by the spin-orbit splitting of the $\tilde{X}(^2E)$ state), namely a pure $3_0^v$ ($v = 6 - 13$) progression involving the $\nu_3$ mode (essentially the C-O stretching mode) and a combination band $3_0^v 6_0^1$ ($v = 5 - 10$) involving the $\nu_3$ and the $\nu_6$ (the methyl rock vibration) modes. This combination band is produced due to the Jahn-Teller effect in the $\tilde{X}$ state. Similar experiments on $CH_3S$ photodissociation through channel (1) found also a pure $3_0^v$ progression (in the ranges $v = 2 - 15$ and $v = 3 - 14$ for the $^2E_{3/2}$ and $^2E_{1/2}$ doublet components of $\tilde{X}(^2E)$, respectively), and a combination band $2_0^1 3_0^v$ (with $v = 3 - 12$ and $v = 4 - 6$ for the $^2E_{3/2}$ and $^2E_{1/2}$ components, respectively).[30] These experiments, as well as previous spectra,[28] indicate that the Jahn-Teller effect for $CH_3S$ is small.

In addition to the experimental studies, some *ab initio* investigations on the ground and excited electronic states of $CH_3O$ and $CH_3S$ have been reported, starting with the pioneering work of Jackels for $CH_3O$.[35,36] Several years later, *ab initio* calculations of the stationary points relevant for the different photodissociation pathways from the $^2A_1$ excited state of both $CH_3O$[37,38] and $CH_3S$[37] were reported. The ground electronic state $^2E$ and its associated Jahn-Teller effect have been investigated in a number of works for $CH_3O$[39,40] and $CH_3S$,[41–43] with and without spin-orbit (SO) coupling. Two-dimensional surfaces in the C-O distance and O-C-H bending angle were calculated for the ground and the three first repulsive excited states (i.e., excluding the bound $^2A_1$ excited state), in order to study the $O(^3P) + CH_3 \rightarrow CH_3O$ reactive scattering process.[44] More recently, *ab initio* full-dimensional calculations of the $^2E$ and $^2A_1$ electronic states were carried out in the Franck-Condon region to simulate the light-induced fluorescence (LIF) $\tilde{A}(^2A_1) \leftarrow \tilde{X}(^2E)$ excitation spectrum

of $CH_3O$ and $CD_3O$.[45] Clearly $CH_3O$ has been more extensively investigated than $CH_3S$ from the theoretical point of view.

Despite the number of *ab initio* works reported in the literature for $CH_3O$, the picture of the potential-energy surfaces involved in the $CH_3O$ photodissociation upon the $\tilde{A}(^2A_1) \leftarrow \tilde{X}(^2E)$ transition is still incomplete. Indeed, many of the previous studies have restricted to the Franck-Condon region because their focus was on investigating either the Jahn-Teller effect or the LIF excitation spectrum, and therefore the asymptotic region of the different electronic PESs was not sampled. Some other works sampled the whole spatial region, including both the interaction and the asymptotic regions, but they lack some of the electronic states involved in the photodissociation process (like the $^2A_1$ state) or they neglect the SO coupling. The situation for $CH_3S$ regarding lack of *ab initio* information is even more dramatic. As a result, it is not possible at present to interpret the photodissociation of $CH_3O$ and $CH_3S$ in terms of the *ab initio* PESs of all the electronic states involved in the process.

The aim of the present work is to report the potential-energy surfaces of all the relevant electronic states involved in the $CH_3X \rightarrow CH_3 + X$ $(X = O, S)$ photodissociation process that takes place upon the $\tilde{A}(^2A_1) \leftarrow \tilde{X}(^2E)$ transition, including the spin-orbit couplings between the corresponding states. Highly correlated *ab initio* methods are used in the calculation of the potential surfaces and couplings. A two-dimensional coordinate representation has been adopted, where the two main modes of the radical molecules, namely the C-X distance and the $CH_3$ umbrella mode (or the H-C-O angle), are considered. These two coordinates are denoted by $R$ and $\theta$, respectively, and are shown in Fig. 1. The C-H distance is denoted by the $r$ coordinate in the figure, and this coordinate is related to the symmetric stretch mode of the $CH_3$ group. In the calculations only $R$ and $\theta$ are varied, while $r$ remains constant at its equilibrium value.

It would be desirable to use a three-dimensional representation including the three coordinates, but this turns out to be too demanding computationally. The

reason to choose the $R$ and $\theta$ coordinates in our two-dimensional representation instead of other possibilities, like the $R$ and $r$ representation, for instance, is that the coupling of the C-X stretch mode with the $CH_3$ umbrella mode is expected to be stronger than with the $CH_3$ symmetric stretch mode. In addition, the separation between the energy levels of the $CH_3$ umbrella mode is much smaller than that of the methyl group symmetric stretch mode Thus, upon fragmentation of the C-X bond, the available energy is more likely to flow to the umbrella mode than to the symmetric stretch mode, producing an internal state distribution of the $CH_3$ fragment in the umbrella vibration that could be described by the $R$ and $\theta$ two-dimensional representation currently chosen.

The paper is organized as follows. In Section 2 the theoretical methodology employed and the computational details are described. In Section 3 the results are presented and discussed. Conclusions are given in Section 4.

## 2. Theoretical background

The electronic structure calculations were performed using the MOLPRO suite of programs.[46,47] In their ground electronic state, both $CH_3O$ and $CH_3S$ present $C_{3v}$ symmetry, as displayed in Fig. 1. Since $C_{3v}$ is not an Abelian group, the *ab initio* calculations were performed using the $C_s$ group representation, which is valid for all the geometries considered in this work. The representations $A_1$ and $A_2$ of the $C_{3v}$ symmetry group give rise to the $A'$ and $A''$ representations in $C_s$, respectively, while the states in the $E$ representation give rise to one $A'$ and one $A''$ degenerate states. The aug-cc-pVQZ basis set of Dunning[48] was used in all the calculations of the surfaces, including *spdfg* basis functions for the C, O, and S atoms and *spdf* basis functions for the H atom.

We are primarily interested in the dissociation of the $CH_3X$ (X=O, S) radical along the C-X stretching coordinate. In order to get the potential-energy curves along this coordinate, geometry optimizations in the ground state of $CH_3X$ were carried out at different R values using the complete active space self-consistent field

(CASSCF) method[49,50] followed by the multireference perturbation theory CASPT2 method.[51] Using the optimized geometries, the ground and excited electronic state energies were computed by means of state-average CASSCF followed by the internally contracted multireference configuration interaction (MRCI) approach.[52] The orbitals included in the active space are 6 $a$ (from $3^{rd}$ to $8^{th}$) and 2 $a$ (from $1^{st}$ to $2^{nd}$ ) for CH3O, and 6 $a$ (from $6^{th}$ to $11^{th}$) and 2 $a$ (from $2^{nd}$ to $3^{rd}$) for CH3S. In order to consider all the states involved in the photodissociation process in the CASSCF wavefunction, the 3 doublet and the 3 quartet states correlating to O/S($\tilde{X}^3P$) + $CH_3(\tilde{X}A_2)$ dissociation channel as well as the 5 doublet states correlating to O/S($1^1D$) + $CH_3(\tilde{X}A_2)$ products were included in the state average. Then, the electronic wave functions of the 4 $^2A'$, the 4 $^2A''$, the $^4A'$, and the two $^4A''$ states were calculated at MRCI level.

Spin-orbit matrix elements were calculated from the MRCI electronic wavefunctions using the Breit-Pauli method implemented in MOLPRO.[53] Taking into account the spin-orbit effects, the 11 states included in our electronic basis gave rise to 28 spin-orbit states which were considered in this work. Out of the 28 S-O states, 20 ones are relevant for the photodissociation process, namely 4 states associated with the electronic ground state $^2E$ ($^2A' + ^2A''$), 2 states associated with the $^2A_1$ bound electronic state, 2 states associated with the $^2A_2$ ($^2A''$) dissociative electronic states, 8 states associated with the $^4E$ ($^4A' + ^4A''$) dissociative electronic state, and 4 states associated with the $^4A_2$ ($^4A''$) dissociative electronic state. The remaining 8 states associated with two $^2E$ electronic states correlate to the O/S($1^1D$) + $CH_3(\tilde{X}A_2)$ dissociation channel and are not expected to play any role in the photodissociation process. They were included in the calculations in order to describe correctly the bound $^2A_2$ state in the asymptotic region where they are degenerated.

In order to investigate the influence of the $CH_3$ umbrella mode on the photodissociation process, two-dimensional calculations of the spin-orbit states as a function of $R$ and $\theta$ were carried out. For $CH_3O$, the calculations sampled geometries over a $24 \times 11$ grid in $R$ and $\theta$, respectively, with the following values: $R$ =[0.5, 0.9, 1.0,

1.1, 1.2, 1.3, 1.4, 1.5, 1.6, 1.7, 1.8, 1.9, 2.0, 2.2, 2.4, 2.6, 2.8, 3.0, 3.2, 3.5, 4.0, 4.5, 5.0, 20] $\mathring{A}$ and $\theta$ = [50, 60, 70, 80, 90, 100, 110, 120, 130, 140, 145] degrees. For $CH_3S$, a grid of $22 \times 11$ was used, taking the shortest value of $R = 1$ Å, since sulfur is bigger than oxygen.

## 3. Results and discussion

The values of the $R$, $\theta$, and $r$ coordinates at the equilibrium configuration in $^2E$ and $^2A_1$ were obtained in this work at the CCSD(T)-F12 (for $^2E$) and MRCI/CASSCF (for $^2A_1$) level of theory with the aug-cc-pVTZ (AVTZ) basis set,[54] using MOLPRO[46] and the default options. In the MRCI/CASSCF calculations of the geometries, all the valence orbitals were employed to define the active space. Whereas the geometry of the $^2A_1$ non-degenerate electronic state was fully optimized without any restriction, the $C_{3v}$ symmetry was imposed in the optimization process of the degenerated ground electronic state favor geometry. The calculated geometries are collected in Table 1, and compared to those reported in some previous works. The agreement with the previous results is excellent.

The equilibrium rotational constants of $CH_3O$ and $CH_3S$ were computed at the MRCI/CASSCF/AVTZ[52] and RCCSD(T)-F12/AVTZ[55,56] levels of theory, and compared to the experimental values when available. For the electronic ground state the $B_e$ rotational constant was calculated with the equation[57,58]

$$B_e = B_e(RCCSD(T) - F12) + \Delta B^{core}(RCCSD(T)), \tag{4}$$

and with similar equations for the constants $A_e$ and $C_e$. In eqn (4) $\Delta B^{core}$ is defined as

$$\Delta B^{core} = B_e(CV) - B_e(V), \tag{5}$$

where $B_e(CV)$ and $B_e(V)$ were calculated correlating both core and valence electrons ($CV$) or just the valence electrons ($V$) in the post SCF process. The effect of the core-electron correlation was determined at the RCCSD(T) level of theory.[59] In order to compare the calculated value with the experimental one of $B_0$ (and also of $A_0$

and $C_0$), the vibrational contribution must be taken into account,

$$B_0 = B_e + \Delta B^{vib}. \tag{6}$$

However, it was not possible to determine accurately the vibrational contribution due to the spin-orbit interaction (the $\tilde{X}(^2E)$ state is a degenerate doublet) and the Jahn-Teller effect. As a result, symmetry and the orbital degeneration are broken, and the optimization options of MOLPRO cannot be used, leading to a lower accuracy of the calculated values. An accurate calculation of the vibrational contribution is out of the scope of this work.

The calculated equilibrium rotational constants for the $\tilde{X}(^2E)$ state of $CH_3O$ at the RCCSD(T)-F12/AVTZ level are $A_e = 158183.50$ MHz and $B_e = C_e = 27671.60$ MHz, while the experimental[19] values are $A_0 = 156068.96$ MHz and $B_0 = 27931.14$ MHz. An estimate of the vibrational contributions led to the result that $\Delta A^{vib} < 0$, $\Delta B^{vib} < 0$, and $\Delta C^{vib} > 0$. Taking into account these trends, the differences between the calculated and the experimental constants for $CH_3O$ are not large. For $CH_3S$ the calculated equilibrium rotational constants are $A_e = 159417.66$ MHz and $B_e = C_e = 13443.95$ MHz with the RCCSD(T)-F12 calculation. There are no experimental values available for $CH_3S$.

Excitation energies, rotational constants, and harmonic frequencies of the different modes have been calculated for the $\tilde{A}(^2A_1)$ state of both $CH_3O$ and $CH_3S$ at the MRCI level. They are collected in Table 2 and compared to the available experimental data. Agreement between the calculated and the experimental magnitudes of Table 2 is very good in general for both radical molecules, particularly for the vertical excitation energies. The agreement is slightly better for $CH_3O$. It is found that the *ab initio* description of the experimental mode frequencies is quite accurate in general, which seems to indicate that the present level of theory used to calculate the potential-energy surfaces and the associated SO couplings is reliable enough. Those potential surfaces and couplings for $CH_3O$ and $CH_3S$ will be discussed in the following.

**Potential-energy surfaces and SO couplings of $CH_3O$**

The potential-energy curves of the ground and the first six excited electronic states of $CH_3O$ as a function of the R distance are displayed in Fig. 2, with and without SO coupling. These are the relevant electronic states involved in the photodissociation process of eqn (1) upon the $\tilde{A}(^2A_1) \leftarrow \tilde{X}(^2E)$ transition. Indeed, after excitation of the $^2A_1$ state, it predissociates to the $^4A_2$, $^2A_2$, and $^4E$ states through SO coupling.

Considering the SO coupling in the calculations has a remarkable effect in the shape of the potential-energy curves which is appreciable even at the large energy scale of Fig. 2. The insets in the two panels of Fig. 2 make possible a more detailed comparison of the shapes of the curves. The change in the shape of the different potential curves (and particularly the modification of the anharmonicity of the $^2A_1$ state) when the SO coupling is considered causes changes in the positions of the minima of the $^2A_1$ bound states, and of the crossing points of $^2A_1$ with the $^4A_2$, $^2A_2$, and $^4E$ repulsive states. Table 3 summarizes the positions of those points when the SO coupling is considered or not.

Table 3 shows that the position of the ground state minimum does not practically change both in energy and C-O distance, upon consideration of the SO coupling. On the contrary, with SO coupling the energy position of the $^2A_1$ state minimum changes remarkably, appearing $\sim 1000$ cm$^{-1}$ higher, at a somewhat shorter, rather similar distance as without SO coupling. The crossing points between $^2A_1$ and the $^4A_2$, $^2A_2$, and $^4E$ states are also modified, occurring at higher energies by $\sim 200$ cm$^{-1}$ and at shorter distances by $\sim 0.04$ $\AA$ when the SO coupling is considered.

The increase of the $^2A_1$ state minimum energy by $\sim 1000$ cm$^{-1}$ with SO coupling has the effect of increasing the corresponding vibrational energies by a similar amount. Since the energy position of the crossing points between $^2A_1$ and the three repulsive states increases only by $\sim 200$ cm$^{-1}$ with SO coupling, the net effect is a variation of $\sim 800$ cm$^{-1}$ of the relative energies between the $^2A_1$ vibrational energies and the three crossing points. Such a variation is expected to have an impact on

the predissociation dynamics of specific vibrational levels of $^2A_1$, and particularly of those located at energies close to the positions of the crossing points.

A way to assess the quality of our *ab initio* calculations is to compare the calculated asymptotic spin-orbit splittings of O($^3P$) to those found experimentally. To this purpose we calculated the spin-orbit splittings of O($^3P_J$) at the distance $R = 50\mathring{A}$, and found the values 0, 157.40, and 239.98 cm$^{-1}$ for $J = 2$, 1, and 0, respectively. Such values are to be compared with the experimental ones[63] of 0, 158.265, and 226.977 cm$^{-1}$ for $J = 2$, 1, and 0, respectively. The agreement between the calculated and the experimental splittings is indeed very good.

It is now interesting to analyze the SO couplings between the $^2A_1$ state and the $^4A_2$, $^2A_2$, and $^4E$ repulsive states. Such couplings are depicted in Fig. 3 as a function of the $R$ coordinate. The strongest coupling in the region of crossing between $^2A_1$ and the repulsive states is that with the $^4E$ state. The coupling with the $^4A_2$ state is the second most intense one (although much weaker than the coupling with $^4E$), and the coupling with $^2A_2$ is the weakest one. A similar result was found in previous *ab initio* calculations.[37] The SO couplings of Fig. 3 provide very useful information about how the predissociation process from the $^2A_1$ state takes place. Indeed, since the first crossing of $^2A_1$ is with $^4A_2$, when low-energy vibrational states are excited in $^2A_1$ predissociation to $^4A_2$ is expected to dominate. As the energy of the vibrational state initially excited increases, predissociation to the $^4E$ state will be the dominant mechanism. Predissociation to $^2A_2$ is expected to be a quite minor mechanism at any excitation energy.

Contour plots of the potential-energy surfaces of the $^2E$, $^2A_1$, $^4A_2$, $^2A_2$, and $^4E$ states considering the SO coupling are displayed in Fig. 4 as a function of the radial and angular modes. Contour plots of the SO couplings between $^2A_1$ and the $^4A_2$, $^2A_2$, and $^4E$ states are also shown in Fig. 5. As reflected in Table 1, the minimum of the $^2E$ ground state is located at $\theta = 110.1°$. The minimum of the excited bound state $^2A_1$ is located at a slightly smaller angle, $\theta \sim 104°$. Thus, upon the $\tilde{A}(^2A_1) \leftarrow \tilde{X}(^2E)$ transition $CH_3O$ undergoes only a slight distortion of

its geometry, both in the radial (see Table 3) and angular coordinates. It is also noted that the spreading of the well of the $^2A_1$ potential surface along the angular coordinate is more limited than that of the $^2E$ state.

The three repulsive states $^4A_2$, $^2A_2$, and $^4E$ display a very similar angular dependence, as expected. The angular spreading of the three surfaces is also very similar, and larger than that of the $^2A_1$ surface. The curves of intersection between the $^2A_1$ surface and those of the $^4A_2$, $^2A_2$, and $^4E$ repulsive states are quite similar and rather constant ($R \sim 2$ Å) with $\theta$, being the intersection curve between $^2A_1$ and $^4A_2$ slightly more separated from the other two (as expected from Fig. 2). The separation between the three curves becomes somewhat larger for angles $\theta < 80°$ and $\theta > 120°$, where the $R$ values of the three intersections decrease slightly.

Regarding the SO couplings of Fig. 5, a rather weak angular dependence is found for the two couplings between $^2A_1$ and the $^2A_2$ and $^4A_2$ states (the two upper panels of Fig. 5), showing the same trend as the intersection curves of Fig. 4, namely the maximum intensity of the coupling occurs at somewhat smaller $R$ values in the regions $\theta < 80°$ and $\theta > 120°$. The most relevant variation of these two couplings takes place along the radial coordinate (see Fig. 3). Interestingly, the most intense SO couplings, those between $^2A_1$ and the $^4E$ states, present a more pronounced angular dependence. Indeed, the lower panels of Fig. 5 show that the maximum of the couplings occurs around $R = 1.8\mathring{A}$ and $\theta \sim 120°$ for the couplings of the left bottom panel, and $R = 1.8\mathring{A}$ and $\theta \sim 130°$ for the couplings of the right bottom panel. These angles are larger than the angle of the minimum of the $^2A_1$ potential surface ($\theta \sim 104°$). The implication is that bending excitation of the vibrational state initially populated in $^2A_1$ would favor sampling the regions of maximum intensity of the $^2A_1 - ^4 E$ SO couplings, thus increasing substantially the efficiency of the $^2A_1 \rightarrow ^4 E$ mechanism of predissociation.

**Potential-energy surfaces and SO couplings of $CH_3S$**

In the following the results obtained for $CH_3S$ will be discussed and compared

with those of $CH_3O$. The one-dimensional potential-energy surfaces of the ground and first excited electronic states of $CH_3S$ vs. $R$ are depicted in Fig. 6, with and without SO coupling. As in $CH_3O$, including the SO coupling in the calculations has a remarkable effect in the shape of the potential-energy curves. Not surprisingly, the spin-orbit effect on the potential curves of $CH_3S$ is substantially larger than in $CH_3O$, as can be observed in the change of shape of the curves of the two panels of Fig. 6.

Table 4 summarizes the positions of the minima and crossing points of the different curves in the case of $CH_3S$ when SO coupling is considered or not. Same as in $CH_3O$, the position of the potential minimum of the $^2E$ ground state is practically unaffected upon consideration of the SO effect. Very similarly as in the case of $CH_3O$, for $CH_3S$ the $^2A_1$ state minimum appears $\sim 1000$ cm$^{-1}$ higher in energy when the SO coupling is considered, and also at a rather similar $R$ distance as without SO coupling. The situation becomes different for the crossing points between $^2A_1$ and the $^4A_2$, $^2A_2$, and $^4E$ states. Indeed, these points appear located $\sim 300$ cm$^{-1}$ higher in energy (vs. $\sim 200$ cm$^{-1}$ higher in $CH_3O$), and at shorter distances by $\sim 0.05$ $\mathring{A}$ (vs. $\sim 0.04$ $\mathring{A}$ in $CH_3O$), when the SO coupling is considered. In addition, a remarkable difference between $CH_3O$ and $CH_3S$ is that the $^2E$ and $^2A_1$ bound states of $CH_3O$ have substantially larger well depths than those of $CH_3S$. Same as in the case of $CH_3O$, we have calculated asymptotic SO splittings of the S($^3P_J$) atom at $R = 50\mathring{A}$. The calculated values of 0, 363.79, and 564.90 cm$^{-1}$ are to be compared to the experimental ones[64] of 0, 396.055, and 573.640 cm$^{-1}$ for $J = 2$, 1, and 0, respectively, showing again very good agreement.

The stronger SO effect found in $CH_3S$ as compared to $CH_3O$ is clearly reflected in the SO couplings between $^2A_1$ and the $^4A_2$, $^2A_2$, and $^4E$ states displayed in Fig. 7 vs. $R$. While the shape of the different coupling curves is qualitatively similar as the corresponding ones in $CH_3O$, the intensity of the $CH_3S$ spin-orbit couplings is more than twice that of the $CH_3O$ couplings. Thus, to obtain a reasonably quantitative and reliable description of the electronic states involved in the photodissociation

induced by the $\tilde{A}(^2A_1) \leftarrow \tilde{X}(^2E)$ transition, including the SO effects appears to be important for both $CH_3O$ and $CH_3S$, but particularly so for the latter system. The $CH_3S$ SO couplings display the same trend as in $CH_3O$, with the $^2A_1 -^4 E$ coupling being the most intense one, followed in intensity by the $^2A_1 -^4 A_2$ coupling. Thus, again the $^2A_1 \rightarrow^4 E$ mechanism of predissociation is expected to be the dominant one in $CH_3S$.

In Fig. 8 contour plots associated with the potential surfaces of the $^2E$, $^2A_1$, $^4A_2$, $^2A_2$, and $^4E$ states considering the SO coupling are displayed as a function of $R$ and $\theta$. The shape of the surfaces is qualitatively very similar to that of the $CH_3O$ surfaces of Fig. 4, leaving aside the above mentioned larger well depth of the $^2E$ and $^2A_1$ surfaces in $CH_3O$. In $CH_3S$ the minimum of the $^2A_1$ state occurs at even a smaller angle, $\theta \sim 99^\circ$, than the equilibrium angle $\theta \sim 110^\circ$ of the $^2E$ ground state than in the case of $CH_3O$ (see Table 1). This means a somewhat larger distortion of the $CH_3S$ geometry upon the $\tilde{A}(^2A_1) \leftarrow \tilde{X}(^2E)$ transition as compared to $CH_3O$. The intersection curves between the $^2A_1$ state and the $^4A_2$, $^2A_2$, and $^4E$ repulsive states display the same trend as in $CH_3O$, but showing a more pronounced angular dependence, particularly the intersection between $^2A_1$ and $^4A_2$. Likewise, the separation of the three intersection curves at $\theta < 80^\circ$ and $\theta > 120^\circ$, is remarkably larger than in $CH_3O$. The implication is that bending excitation of the initial state excited in $^2A_1$ is expected to produce a larger discrimination between the two main mechanisms of predissociation, $^2A_1 \rightarrow^4 E$ and $^2A_1 \rightarrow^4 A_2$, than in $CH_3O$.

Contour plots of the different SO couplings of $CH_3S$ are presented in Fig. 9. They are also similar in shape to those of $CH_3O$ shown in Fig. 5, although more intense. Again, the couplings between $^2A_1$ and the $^2A_2$ and $^4A_2$ states display a rather weak angular dependence. The $^2A_1 -^4 E$ SO couplings display two maxima, around $R = 2.2\mathring{A}$ and $\theta = 60^\circ$ and $R = 2.0\mathring{A}$ and $\theta = 134^\circ$ for the left bottom panel, and around $R = 2.2\mathring{A}$ and $\theta = 60^\circ$ and $R = 2.0\mathring{A}$ and $\theta = 130^\circ$ for the right bottom panel. As a result of this angular shift of the maxima of the SO couplings to remarkably higher and lower angles than the $^2A_1$ equilibrium angle, the effect of

initial bending excitation in increasing the efficiency of the $^2A_1 \rightarrow ^4 E$ mechanism of predissociation is expected to be even larger than in $CH_3O$.

Before concluding, it is interesting to point out that the excited electronic states of $CH_3O$ and $CH_3S$ present the same structure as those of the diatomic radicals OH[65] and SH.[66] This is not surprising since both H and $CH_3$ present a single free electron that will lead to a similar covalent bond with the oxygen and sulfur atoms. As a consequence, the ground state of both $CH_3X$ and XH (X=O, S) is characterized by the presence of 3 electrons delocalized in two degenerated HOMO orbitals of $\Pi$ character. Since the first excited states are obtained by promoting an electron from lower orbitals to fill the $\Pi$ orbitals, the dominating electronic configurations of the excited states are similar for XH and $CH_3X$, the only difference being that the linear symmetry of the diatomic molecule is no longer present due to the methyl radical in $CH_3X$. This allows one to establish a direct correlation between the states corresponding to the irreducible representations of $C_{3v}$ and $C_{\infty v}$ symmetry groups. Through this correlation it appears clearly that the doubly degenerate $^2\Pi$ ground state of XH becomes a doubly degenerate $^2E$ state for $CH_3X$. Similarly, the $^2\Sigma^+$ converts into $^2A_1$, the $^4\Sigma^-$ and $^2\Sigma^-$ convert into $^4A_2$ and $^2A_2$, respectively, and $^4\Pi$ becomes a $^4E$ state. From this analogy we can expect qualitatively similar results for the dissociation of XH and $CH_3X$ radicals. However, due to the larger number of degrees of freedom of $CH_3X$, more complex photodissociation dynamics is to be expected in this latter case.

## 4. Summary and conclusions

All the electronic states and the spin-orbit couplings between them involved in the photodissociation process $CH_3X \rightarrow CH_3 + X(X = O, S)$ that occurs upon the $\tilde{A}(^2A_1) \leftarrow \tilde{X}(^2E)$ transition, have been investigated through highly correlated *ab initio* methods. A coordinate representation including two degrees of freedom, namely the C-X dissociative coordinate and the O-C-H bending angle, was used. The present representation of all the electronic states and couplings involved allows

for the first complete description of the above photodissociation process, and opens the possibility of carrying out dinamics simulations. It is found that spin-orbit effects have an important impact on the shape of the excited potential-energy surfaces. This is particularly true for $CH_3S$, which presents spin-orbit couplings with an intensity more than twice that of the $CH_3O$ couplings. Therefore, spin-orbit effects need to be considered in the calculations in order to obtain a reliable representation of the states involved in the photodissociation. Based on the present potential-energy surfaces and on the intensity of the different couplings obtained, the mechanisms of photodissociation are discussed. In particular, bending excitation of the vibrational state initially excited in $\tilde{A}(^2A_1)$ may favor the specific $^2A_1 \rightarrow^4 E$ mechanism of predissociation vs. the other ones.

## Acknowledgments

This work has been supported by MINECO (Spain) (grants No. CTQ2015-65033-P and FIS201340626P) and EU COST Action CM1401 as well as the European Research Council under the European Unions Seventh Framework Programme (FP/2007-2013)/ERC Grant Agreement No. 610256 (NANOCOSMOS). This research has been carried out within the Unidad Asociada Química Física Molecular between the Departamento de Química Física of Universidad Complutense de Madrid (UCM) and Consejo Superior de Investigaciones Cientficas (CSIC). AB acknowledges the financial support of the Tunisian Ministry of Higher Education, Scientific Research, and Technology, of the Short Term Scientific Mission (STSM) program of the COST Action CM1401, and of LSAMA at the Université de Tunis El Manar, that made possible research visits to the Instituto de Física Fundamental (CSIC). The Centro de Supercomputación de Galicia (CESGA, Spain) and CTI (CSIC) are acknowledged for the use of their resurces.

## Notes and references

(1) D. G. Hemdry, *J. Phys. Chem.*, 1977, **81**, 2483.

(2) A. C. Aikin, *J. Geophys. Res.*, 1982, **87**, 3105.

(3) C. K. Westbrook and F. L. Dryer, *Prog. Energy Combust. Sci.*, 1984, **10**, 1.

(4) B. J. Finlayson and J. N. Pitts, *Atmospheric Chemistry*, Wiley, New York, 1986.

(5) D. Perner et al., *J. Atmos. Chem.*, 1987, **5**, 185.

(6) S. Zabarnick, *Combust. Flame*, 1991, **85**, 27.

(7) B. A. Williams and J. W. Flemming, *Chem. Phys. Lett.*, 1994, **221**, 27.

(8) J. H. Seinfeld and S. N. Pandis, *Atmospheric Chemistry and Physics: From Air Pollution to Climate Change*, Wiley, New York, 1998.

(9) D. Grosjean and R. Lewis, *Geophys. Res. lett.*, 1982, **9**, 1203.

(10) S. Hatakeyama and H. Akimoto, *J. Phys. Chem.*, 1983, **87**, 2387.

(11) H. Niki, P. D. Maker, C. M. Savage, and L. P. Breitenbach, *Int. J. Chem. Kinet.*, 1983, **15**, 647.

(12) R. J. Charlson, J. E. Lovelock, M. O. Andreae, and S. G. Warren, *Nature (London)*, 1987, **326**, 655.

(13) H. R. Wendt and H. E. Hunziker, *J. Chem. Phys.*, 1979, **71**, 5202.

(14) G. Inoue, H. Akimoto, and M. Okuda, *J. Chem. Phys.*, 1980, **72**, 1769.

(15) S. D. Brossard, P. G. Carrick, E. L. Chappell, S. C. Hulegaard, and P. C. Engelking, *J. Chem. Phys.*, 1986, **84**, 2459.

(16) X. Liu, C. P. Damo, T.-Y. D. Lin, S. C. Foster, P. Misra, L. Yu, and T. A. Miller, *J. Phys. Chem.*, 1989, **93**, 2266.

(17) D. L. Osborn, D. J. Leahy, E. M. Ross, and D. M. Neumark, *Chem. Phys. Lett.*, 1997, **235**, 484.

(18) D. L. Osborn, D. J. Leahy, and D. M. Neumark, *J. Phys. Chem.*, 1997, **101**, 6583.

(19) D. E. Powers, M. B. Pushkarsky, and T. A. Miller, *J. Chem. Phys.*, 1997, **106**, 6863.

(20) D. E. Powers, M. B. Pushkarsky, and T. A. Miller, *J. Chem. Phys.*, 1997, **106**, 6878.

(21) K. Ohbayashi, H. Akimoto, and I. Tanaka, *Chem. Phys. Lett.*, 1977, **52**, 47.

(22) P. C. Engelking, G. B. Ellison, and W. C. Lineberger, *J. Chem. Phys.*, 1978, **69**, 1826.

(23) B. K. Janousek and J. I. Brauman, *J. Chem. Phys.*, 1980, **72**, 694.

(24) M. Suzuki, G. Inoue, and H. Akimoto, *J. Chem. Phys.*, 1984, **81**, 5405.

(25) Y. Endo, S. Saito, and E. Hirota, *J. Chem. Phys.*, 1986, **85**, 1770.

(26) Y.-C. Hsu, X. Liu, and T. A. Miller, *J. Chem. Phys.*, 1989, **90**, 6852.

(27) C. Anastasi, M. Broomfield, O. J. Nielsen, and P. Pagsberg, *Chem. Phys. Lett.*, 1991, **182**, 643.

(28) S.-Y. Chiang and Y.-P. Lee, *J. Chem. Phys.*, 1991, **95**, 66.

(29) C.-W. Hsu, C.-L. Liao, Z.-X. Ma, P. J. H. Tjossem, and C. Y. Ng, *J. Chem. Phys.*, 1992, **97**, 6283.

(30) R. T. Bise, H. Choi, H. B. Pedersen, D. H. Mordaunt, and D. M. Neumark, *J. Chem. Phys.*, 1999, **110**, 805.

(31) M. B. Pushkarsky, B. E. Applegate, and T. E. Miller, *J. Chem. Phys.*, 2000, **113**, 9649.

(32) G. Balerdi, J. Woodhouse, A. Zanchet, R. de Nalda, M. L. Senent, A. García-Vela and L. Bañares, *Phys. Chem. Chem. Phys.*, 2016, **18**, 110.

(33) S. Marggi Poullain, D. V. Chicharro, A. Zanchet, M. G. González, L. Rubio-Lago, M. L. Senent, A. García-Vela and L. Bañares, *Phys. Chem. Chem. Phys.*, 2016, **18**, 17054.

(34) A. Zanchet, L. Bañares, M. L. Senent, and A. García-Vela, *Phys. Chem. Chem. Phys.*, 2016, **18**, 33195.

(35) C. F. Jackels, *J. Chem. Phys.*, 1982, **76**, 505.

(36) C. F. Jackels, *J. Chem. Phys.*, 1985, **82**, 311.

(37) Q. Cui and K. Morokuma, *Chem. Phys. Lett.*, 1996, **263**, 54.

(38) N. D. K. Petraco, W. D. Allen, and H. F. Schaefer III, *J. Chem. Phys.*, 2002, **116**, 10229.

(39) U. Höper, P. Botschwina, and U. Köppel, *J. Chem. Phys.*, 2000, **112**, 4132.

(40) A. V. Marenich and J. E. Boggs, *J. Chem. Phys.*, 2005, **122**, 024308.

(41) T. A. Barckholtz and T. A. Miller, *J. Phys. Chem. A*, 1999, **103**, 2321.

(42) A. V. Marenich and J. E. Boggs, *J. Phys. Chem. A*, 2004, **108**, 10594

(43) A. V. Marenich and J. E. Boggs, *J. Chem. Theory Comput.*, 2005, **1**, 1162.

(44) K. Yagi, T. Takayanagi, T. Taketsugu, and K. Hirao, *J. Chem. Phys.*, 2004, **120**, 10395.

(45) J. Nagesh, E. L. Sibert III, and J. F. Stanton, *Spectrochim. Acta Part A: Mol. Biomol.*, 2014, **119**, 90.

(46) H.-J. Werner, P. J. Knowles, *et al., MOLPRO version 2012.1, a package of ab initio programs*, see http://www.molpro.net.

(47) H.-J. Werner, P. J. Knowles, G. Knizia, F. R. Manby, and M. Schutz, *WIREs Comput. Mol. Sci.*, 2012, **2**, 242.

(48) T. H. Dunning, *J. Chem. Phys.*, 1989, **90**, 1007.

(49) H.-J. Werner and P. J. Knowles, *J. Chem. Phys.*, 1985, **82**, 5053.

(50) P. J. Knowles and H.-J. Werner, *Chem. Phys. Lett.*, 1985, **115**, 259.

(51) H.-J. Werner, *Mol. Phys.*, 1996, **89**, 645.

(52) H.-J. Werner and P. J. Knowles, *J. Chem. Phys.*, 1988, **89**, 5803.

(53) A. Berning, M. Schweizer, H.-J. Werner, P. J. Knowles, and P. Palmieri, *Mol. Phys.*, 2000, **98**, 1823.

(54) D. E. Woon, and T. H. Dunning Jr., *J. Chem. Phys.*, 1994, **100**, 2975.

(55) H.-J. Werner, T. B. Adler, and F. R. Manby, *J. Chem. Phys.*, 2007, **126**, 164102.

(56) G. Knizia, T. B. Adler, and H.-J. Werner, *J. Chem. Phys.*, 2009, **130**, 054104.

(57) R. Boussesi, M. L. Senent, and N. Jaïdane, *J. Chem. Phys.*, 2016, **144**, 164110.

(58) S. Dalbouha, M. L. Senent, N. Komiha, and R. Domínguez-Gómez, *J. Chem. Phys.*, 2016, **145**, 124309.

(59) P. J. Knowles, C. Hampel, and H.-J. Werner, *J. Chem. Phys.*, 1993 **99**, 5219.

(60) J. Liu, M.-W. Chen, D. Melnik, J. T. Yi, and T. A. Miller, *J. Chem. Phys.*, 2009, **130**, 074302.

(61) C.-P. Liu, S. A. Reid, and Y.-P. Lee, *J. Chem. Phys.*, 2005, **122**, 124313.

(62) C.-P. Liu, Y. Matsuda, and Y.-P. Lee, *J. Chem. Phys.*, 2003, **119**, 12335.

(63) C. E. Moore, *CRC Series in Evaluated Data in Atomic Physics*, Edited by J. W. Gallagher, CRC Press, Boca Raton, FL, 1993.

(64) W. C. Martin, R. Zalubas, and A. Musgrove, *J. Phys. Chem. Ref. Data*, 1990, **19**, 821.

(65) E. F. van Dishoeck and A. Dalgarno, *J. Chem. Phys.*, 1983, **79**, 873.

(66) W. Zhou, Y. Yuan, S. Chen, and J. Zhang, *J. Chem. Phys.*, 2005, **123**, 054330.

## FIGURE CAPTIONS

Fig. 1 Schematic picture of the equilibrium geometry of both $CH_3O$ and $CH_3S$ that displays $C_{3v}$ symmetry. The coordinate representation used in the *ab initio* calculations is also shown in the figure.

Fig. 2 (a) Potential-energy curves vs. $R$ of the ground and first excited electronic states involved in the $CH_3O$ photodissociation process that takes place upon the $\tilde{A}(^2A_1) \leftarrow \tilde{X}(^2E)$ transition, when the SO coupling between the $^2A_1$ bound state and the $^4A_2$, $^2A_2$, and $^4E$ repulsive states is considered. (b) The same potential-energy curves as in (a) when the SO coupling is not considered. An inset within each panel shows in more detail the excited electronic states.

Fig. 3 Spin-orbit couplings between the $^2A_1$ state and the $^4A_2$, $^2A_2$, and $^4E$ repulsive states vs. $R$ for $CH_3O$. The figure shows the calculated *ab initio* points along with the curves joining them. Only the nonzero couplings between the $^2A_1$ state and the corresponding $^4A_2^{J,M_J}$, $^2A_2^{J,M_J}$, and $^4E^{J,M_J}$ components are shown. The couplings to the degenerate components $^4E^{3/2,3/2}$ and $^4E^{3/2,1/2}$ (and similarly with the degenerate components $^4E^{3/2,-3/2}$ and $^4E^{3/2,-1/2}$) are identical.

Fig. 4 Contour plots of the $CH_3O$ potential-energy surfaces associated with the $^2E$ ground state, and the $^2A_1$, $^2A_2$, $^4E$, and $^4A_2$ excited states as a function of the $R$ and $\theta$ coordinates, when the SO coupling is considered. The intersections of the $^2A_1$ state with the $^2A_2$ (solid line), $^4E$ (dashed line), and $^4A_2$ (dotted line) states are also shown in the panels.

Fig. 5 Contour plots of the spin-orbit couplings between $^2A_1$ and the $^2A_2^{1/2,1/2}$ state, the $^4A_2^{3/2,1/2}$ state, the $^4E^{3/2,3/2}$ and $^4E^{3/2,1/2}$ states, and the $^4E^{3/2,-3/2}$ and $^4E^{3/2,-1/2}$ states, as a function of the $R$ and $\theta$ coordinates for $CH_3O$.

Fig. 6 Same as Fig. 2 but for $CH_3S$.

Fig. 7 Same as Fig. 3 but for $CH_3S$.

Fig. 8 Same as Fig. 4 but for $CH_3S$.

Fig. 9 Same as Fig. 5 but for $CH_3S$.

## TABLE CAPTIONS

Table 1 Equilibrium geometries obtained in this work for the minima associated with the $\tilde{X}(^2E)$ and $\tilde{A}(^2A_1)$ bound states, and compared with those found in previous works. See the text for details.

Table 2 Vertical excitation energies, $E$ (from the $^2E$ state), rotational constants, and fundamental frequencies of the different modes calculated at the CASSCF/AVTZ level for the $^2A_1$ state of $CH_3O$ and $CH_3S$. The corresponding available experimental values are also collected in the table for comparison.

Table 3 Energies and $R$ distances associated with the minima of the $^2E$ and $^2A_1$ bound states and with the crossing points between the $^2A_1$ state and the repulsive $^4A_2$, $^2A_2$, and $^4E$ states for $CH_3O$, both with and without SO coupling.

Table 4 Same as Table 3, but for $CH_3S$.

TABLE 1

| System | State | $R$ (Å) | $r$ (Å) | $\theta(deg)$ |
|---|---|---|---|---|
| $CH_3O^a$ | $\tilde{X}(^2E)$ | 1.378 | 1.096 | 110.1 |
| $CH_3O^b$ | $\tilde{X}(^2E)$ | 1.374 | 1.094 | 110.3 |
| $CH_3O^a$ | $\tilde{A}(^2A_1)$ | 1.574 | 1.086 | 103.1 |
| $CH_3O^c$ | $\tilde{A}(^2A_1)$ | 1.573 | 1.085 | 103.1 |
| $CH_3S^a$ | $\tilde{X}(^2E)$ | 1.798 | 1.089 | 109.7 |
| $CH_3S^d$ | $\tilde{X}(^2E)$ | 1.794 | 1.088 | 109.8 |
| $CH_3S^a$ | $\tilde{A}(^2A_1)$ | 2.114 | 1.083 | 98.9 |
| $CH_3S^d$ | $\tilde{A}(^2A_1)$ | 2.064 | 1.079 | 99.8 |

[a]This work.

[b]Ref. [40].

[c]Ref. [45].

[d]Ref. [43].

TABLE 2

| $CH_3O$ | | | $CH_3S$ | | |
|---|---|---|---|---|---|
| | MRCI | Exp. | | MRCI | Exp. |
| E ($cm^{-1}$) | 31777 | 31644.2[a] | E ($cm^{-1}$) | 26841 | 26396.8[c] |
| $A_e$ (MHz) | 149320.52 | | $A_e$ (MHz) | 146124.35 | |
| $B_e$=$C_e$ (MHz) | 22710.58 | | $B_e$=$C_e$ (MHz) | 10327.23 | |
| $\nu_1(a_1)$ $CH_3$ st ($cm^{-1}$) | 3055 | 2947.8[b] | $\nu_1(a_1)$ $CH_3$ st ($cm^{-1}$) | 3092 | 2940[c] |
| $\nu_2(a_1)$ umb ($cm^{-1}$) | 1351 | 1289.3[b] | $\nu_2(a_1)$ umb ($cm^{-1}$) | 1155 | 1095.9[c] |
| $\nu_3(a_1)$ CO st ($cm^{-1}$) | 710 | 662.4[b] | $\nu_3(a_1)$ CS st ($cm^{-1}$) | 418 | 401 $\pm$2[c] |
| $\nu_4(E)$ $CH_3$ st ($cm^{-1}$) | 3203 | 3077.8[b] | $\nu_4(E)$ $CH_3$ st ($cm^{-1}$) | 3263 | 3006[d] |
| $\nu_5(E)$ $CH_2$ sc ($cm^{-1}$) | 1464 | 1403.0[b] | $\nu_5(E)$ $CH_2$ sc ($cm^{-1}$) | 1444 | |
| $\nu_6(E)$ HCO def ($cm^{-1}$) | 996 | 929.5[b] | $\nu_6(E)$ HCS def ($cm^{-1}$) | 670 | 635 $\pm$10[e] |

(st= stretch, umb=umbrella, sc=scissors, def=deformation)

[a]Ref. [60].

[b]Ref. [19].

[c]Ref. [61].

[d]Ref. [62].

[e]Ref. [28].

TABLE 3

| With SO coupling | | |
|---|---|---|
| State | Energy ($cm^{-1}$) | $R$ (Å) |
| $^2E$ | -30900 | 1.378 |
| $^2A_1$ | 1058 | 1.520 |
| $^4A_2$ | 7371 | 2.010 |
| $^4E$ | 8490 | 2.077 |
| $^2A_2$ | 8644 | 2.087 |
| Without SO coupling | | |
| State | Energy ($cm^{-1}$) | $R$ (Å) |
| $^2E$ | -30859 | 1.378 |
| $^2A_1$ | 73 | 1.549 |
| $^4A_2$ | 7125 | 2.056 |
| $^4E$ | 8300 | 2.121 |
| $^2A_2$ | 8456 | 2.130 |

TABLE 4

| With SO coupling | | |
|---|---|---|
| State | Energy ($cm^{-1}$) | $R$ (Å) |
| $^2E$ | -25131 | 1.798 |
| $^2A_1$ | 2327 | 2.120 |
| $^4A_2$ | 4295 | 2.486 |
| $^2A_2$ | 5091 | 2.593 |
| $^4E$ | 5.114 | 2.597 |
| Without SO coupling | | |
| State | Energy ($cm^{-1}$) | $R$ (Å) |
| $^2E$ | -25140 | 1.798 |
| $^2A_1$ | 1340 | 2.100 |
| $^4A_2$ | 4016 | 2.535 |
| $^2A_2$ | 4798 | 2.637 |
| $^4E$ | 4922 | 2.656 |

**Fig. 1**

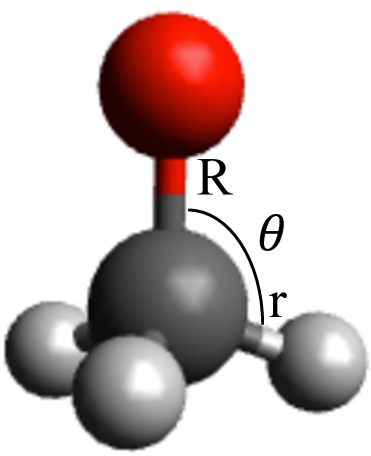

**Fig.2**

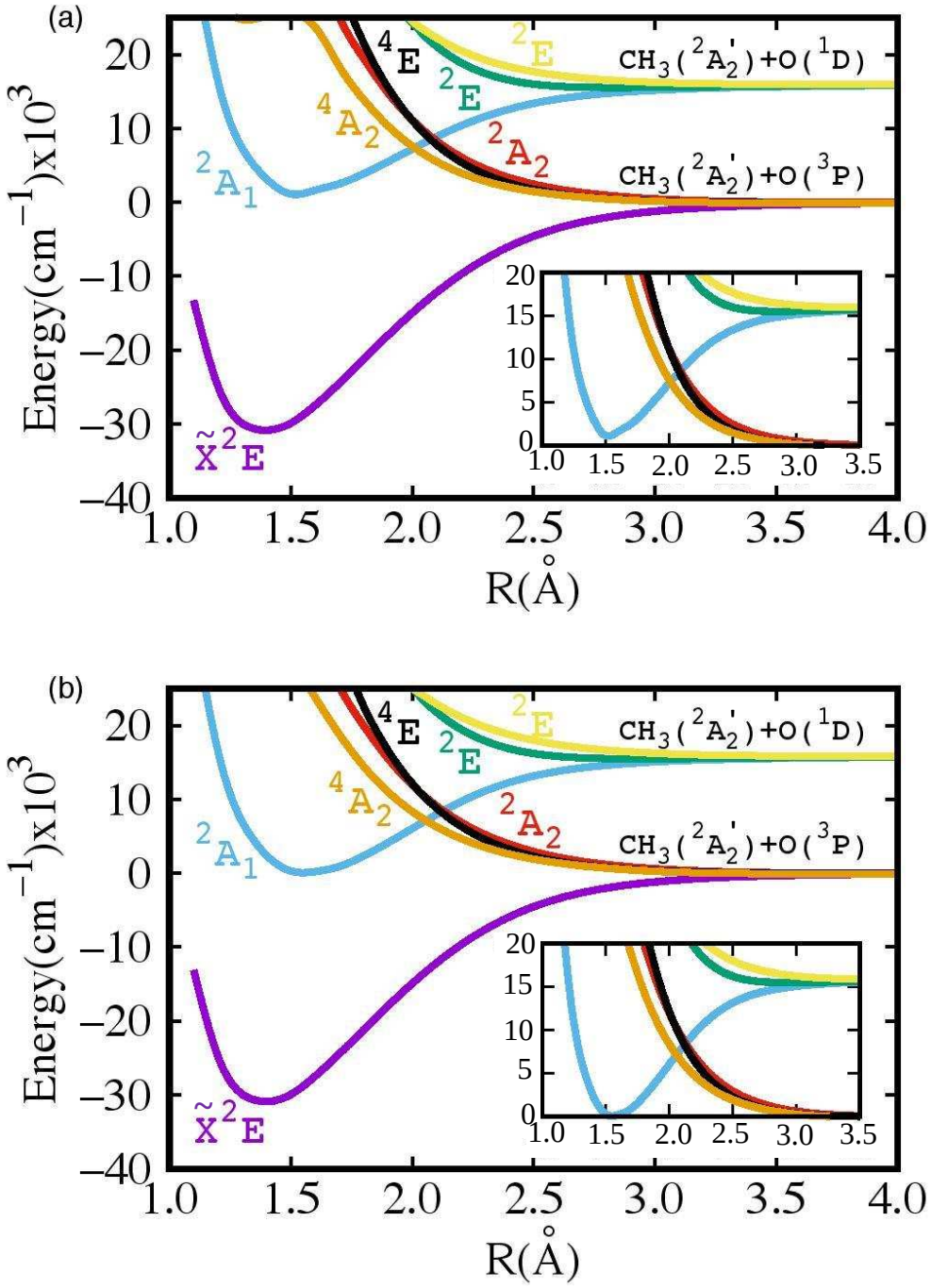
(a)
(b)
Energy(cm$^{-1}$)x10$^3$
R(Å)
$^4$E
$^2$E
$^2$E
$^4$A$_2$
$^2$A$_2$
$^2$A$_1$
$\tilde{X}^2$E
CH$_3$($^2$A$_2'$)+O($^1$D)
CH$_3$($^2$A$_2'$)+O($^3$P)

**Fig. 3**

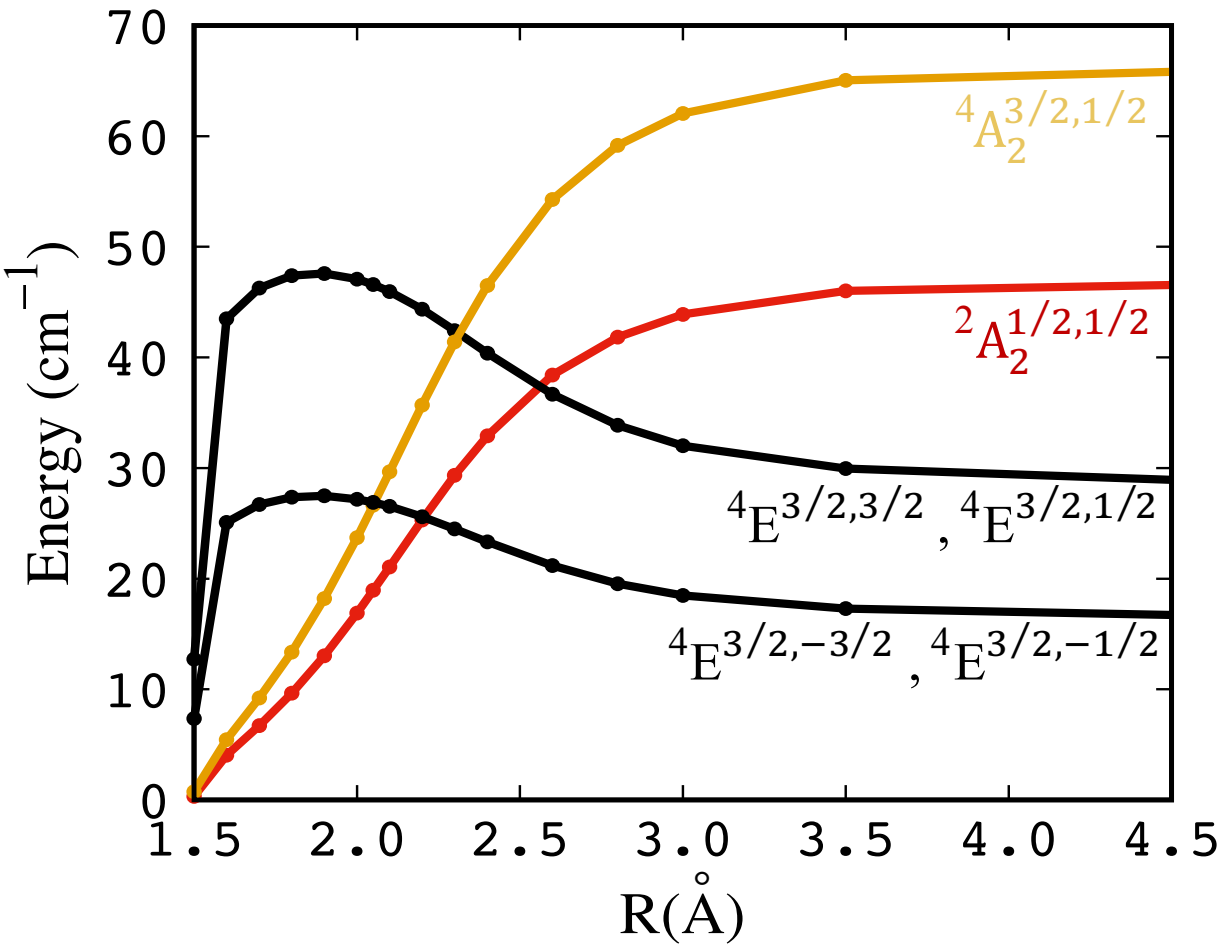
70
60
50
40
30
20
10
0
Energy (cm$^{-1}$)
1.5
2.0
2.5
3.0
3.5
4.0
4.5
R(Å)
$^4A_2^{3/2,1/2}$
$^2A_2^{1/2,1/2}$
$^4E^{3/2,3/2}$ , $^4E^{3/2,1/2}$
$^4E^{3/2,-3/2}$ , $^4E^{3/2,-1/2}$

Fig. 4

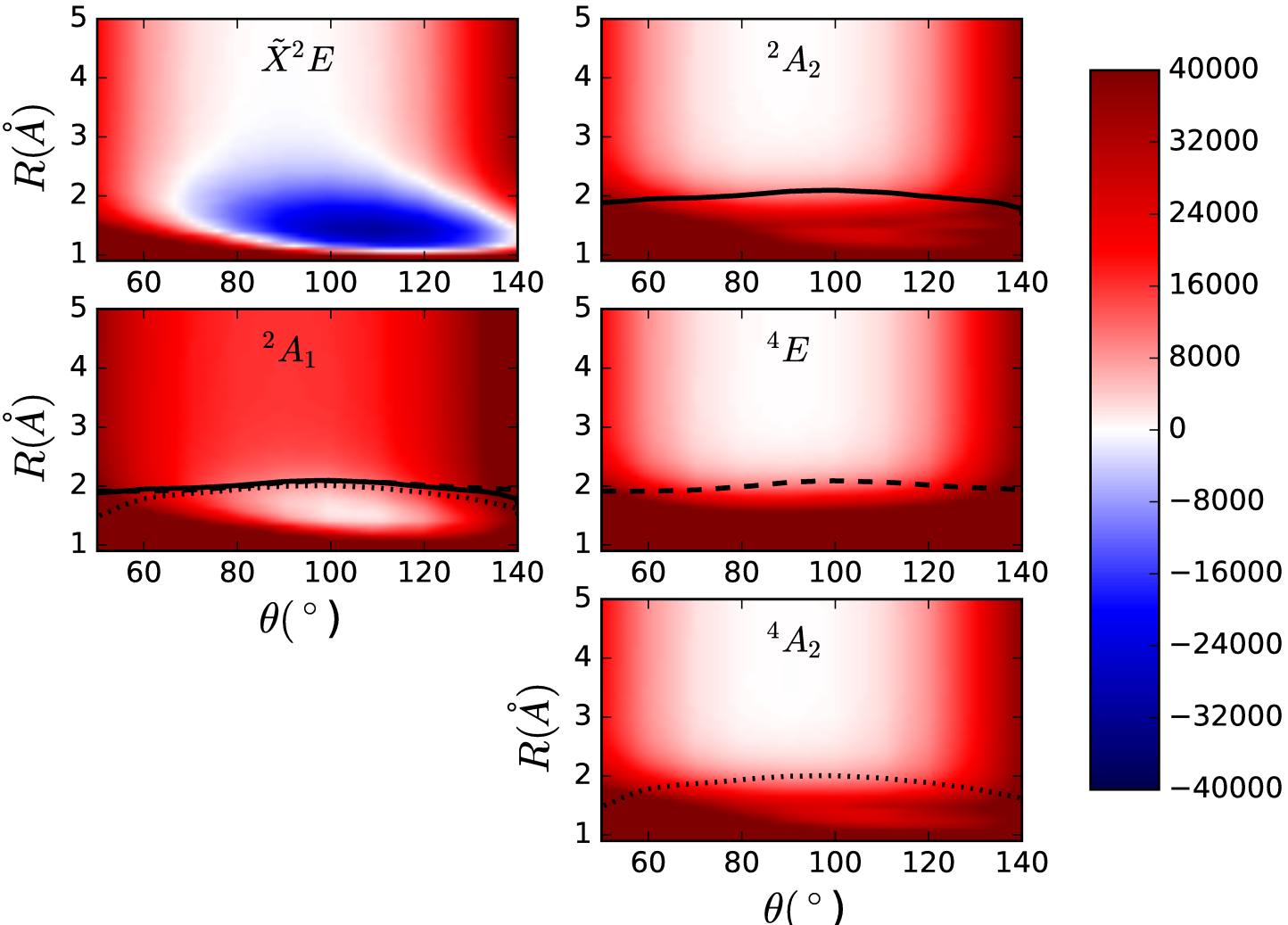
$\tilde{X}^2E$
$^2A_2$
$^2A_1$
$^4E$
$^4A_2$
$R(\mathring{A})$
$\theta(^\circ)$
1
2
3
4
5
60
80
100
120
140
40000
32000
24000
16000
8000
0
−8000
−16000
−24000
−32000
−40000

Fig. 5

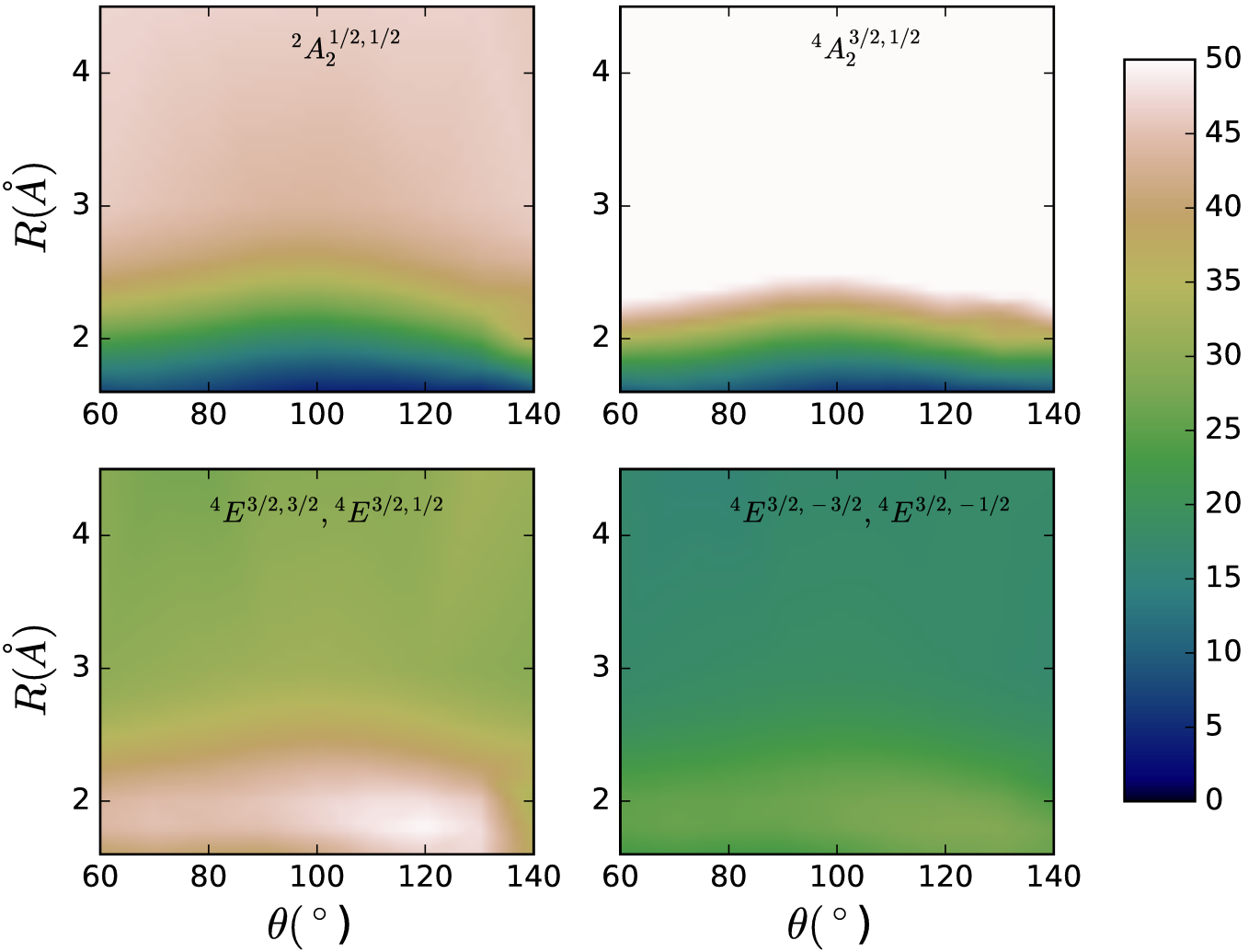
$^2A_2^{1/2,1/2}$
$^4A_2^{3/2,1/2}$
$^4E^{3/2,3/2}, ^4E^{3/2,1/2}$
$^4E^{3/2,-3/2}, ^4E^{3/2,-1/2}$
$R(\mathring{A})$
$\theta(^\circ)$
60
80
100
120
140
2
3
4
0
5
10
15
20
25
30
35
40
45
50

**Fig.6**

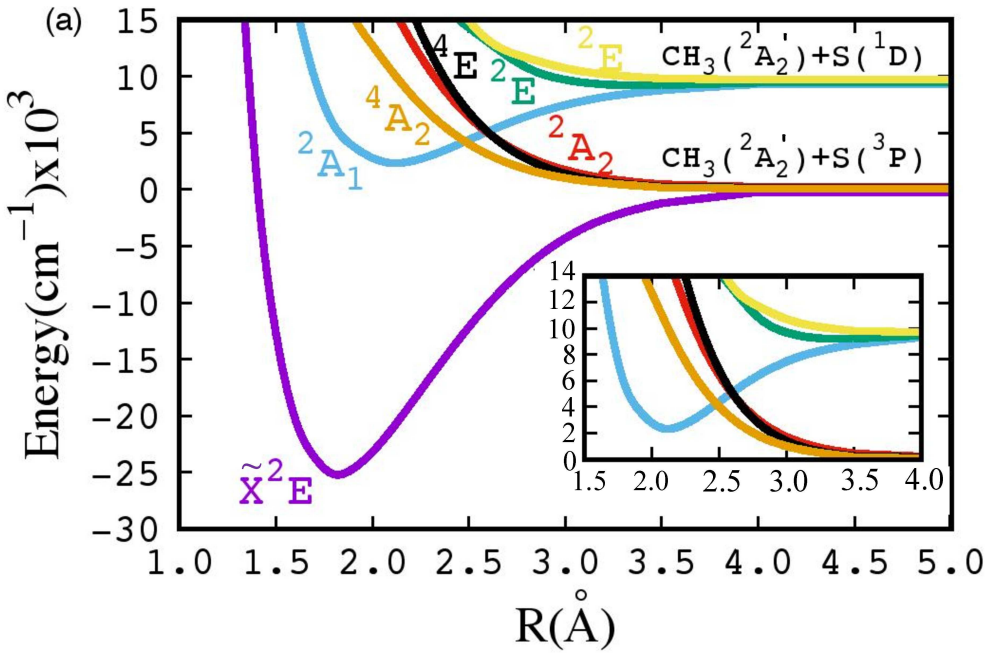
(a)
Energy(cm$^{-1}$)x10$^3$
R(Å)
$^2$E
CH$_3$($^2$A$_2'$)+S($^1$D)
$^4$E
$^2$E
$^4$A$_2$
$^2$A$_2$
CH$_3$($^2$A$_2'$)+S($^3$P)
$^2$A$_1$
$\tilde{X}^2$E

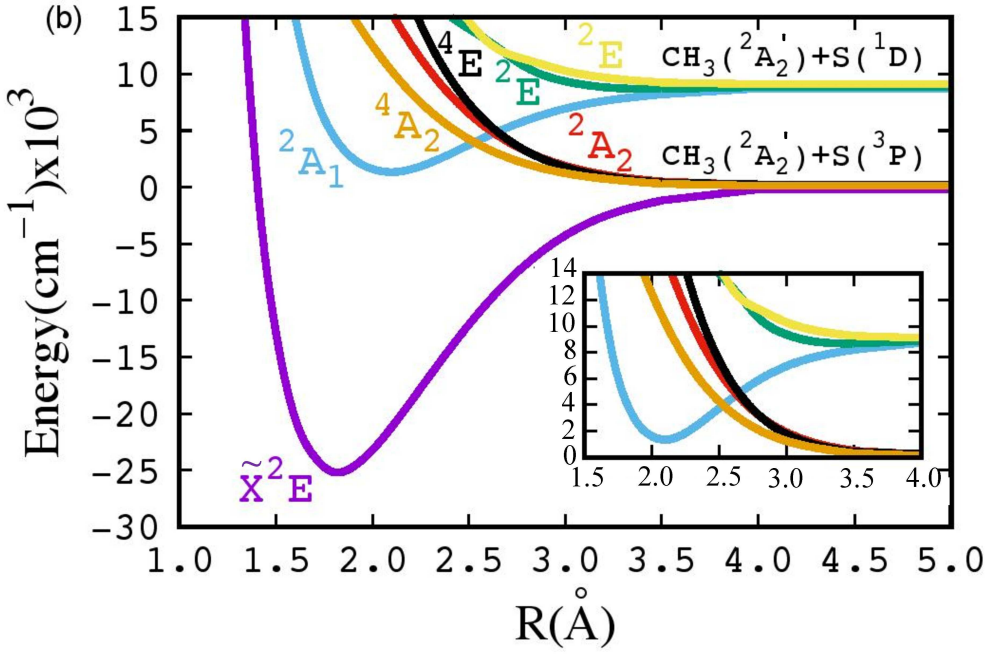
(b)
Energy(cm$^{-1}$)x10$^3$
R(Å)
$^2$E
CH$_3$($^2$A$_2'$)+S($^1$D)
$^4$E
$^2$E
$^4$A$_2$
$^2$A$_2$
CH$_3$($^2$A$_2'$)+S($^3$P)
$^2$A$_1$
$\tilde{X}^2$E

**Fig. 7**

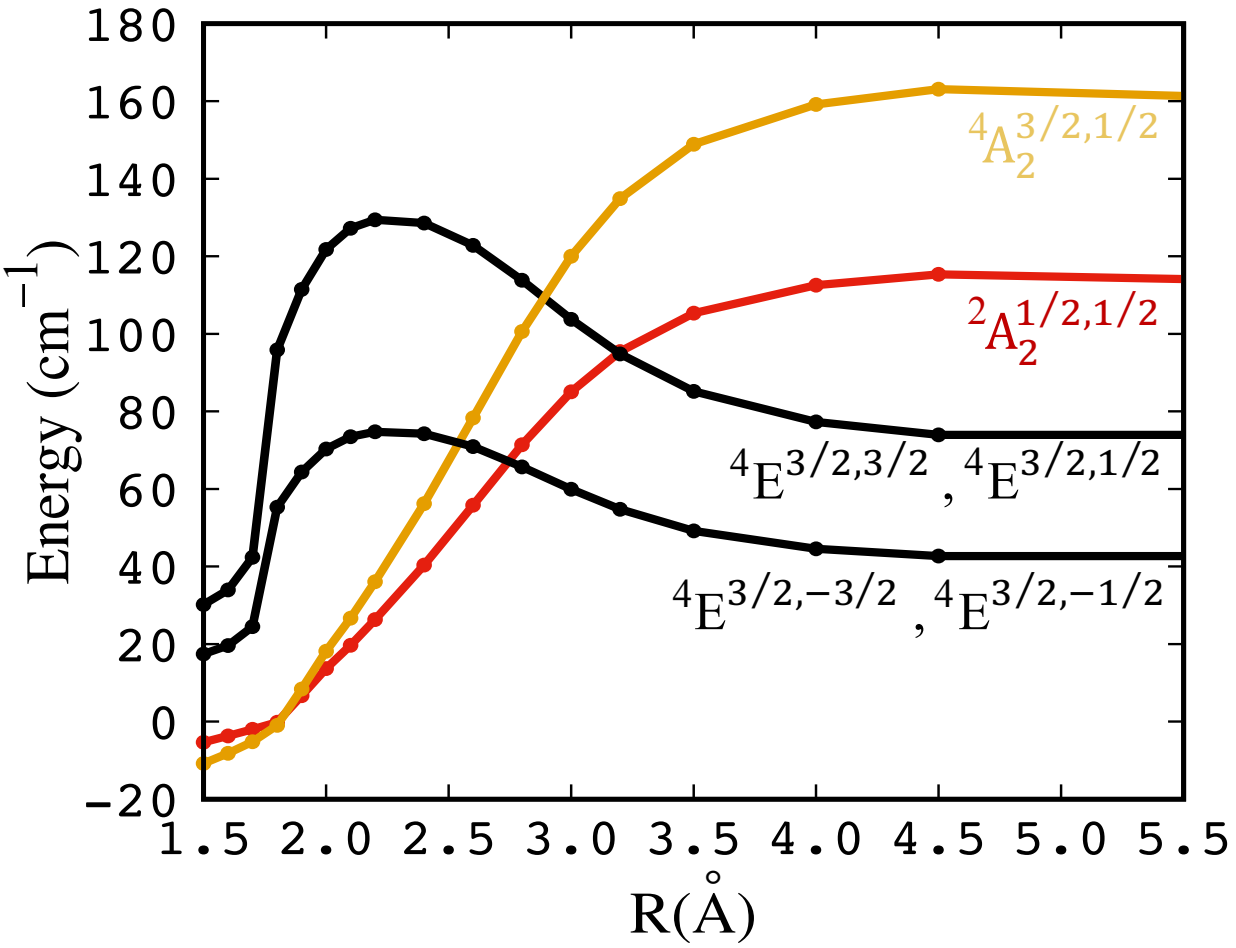
180
160
140
120
100
80
60
40
20
0
−20
Energy (cm$^{-1}$)
1.5
2.0
2.5
3.0
3.5
4.0
4.5
5.0
5.5
R(Å)
$^4A_2^{3/2,1/2}$
$^2A_2^{1/2,1/2}$
$^4E^{3/2,3/2}$ , $^4E^{3/2,1/2}$
$^4E^{3/2,-3/2}$ , $^4E^{3/2,-1/2}$

Fig. 8

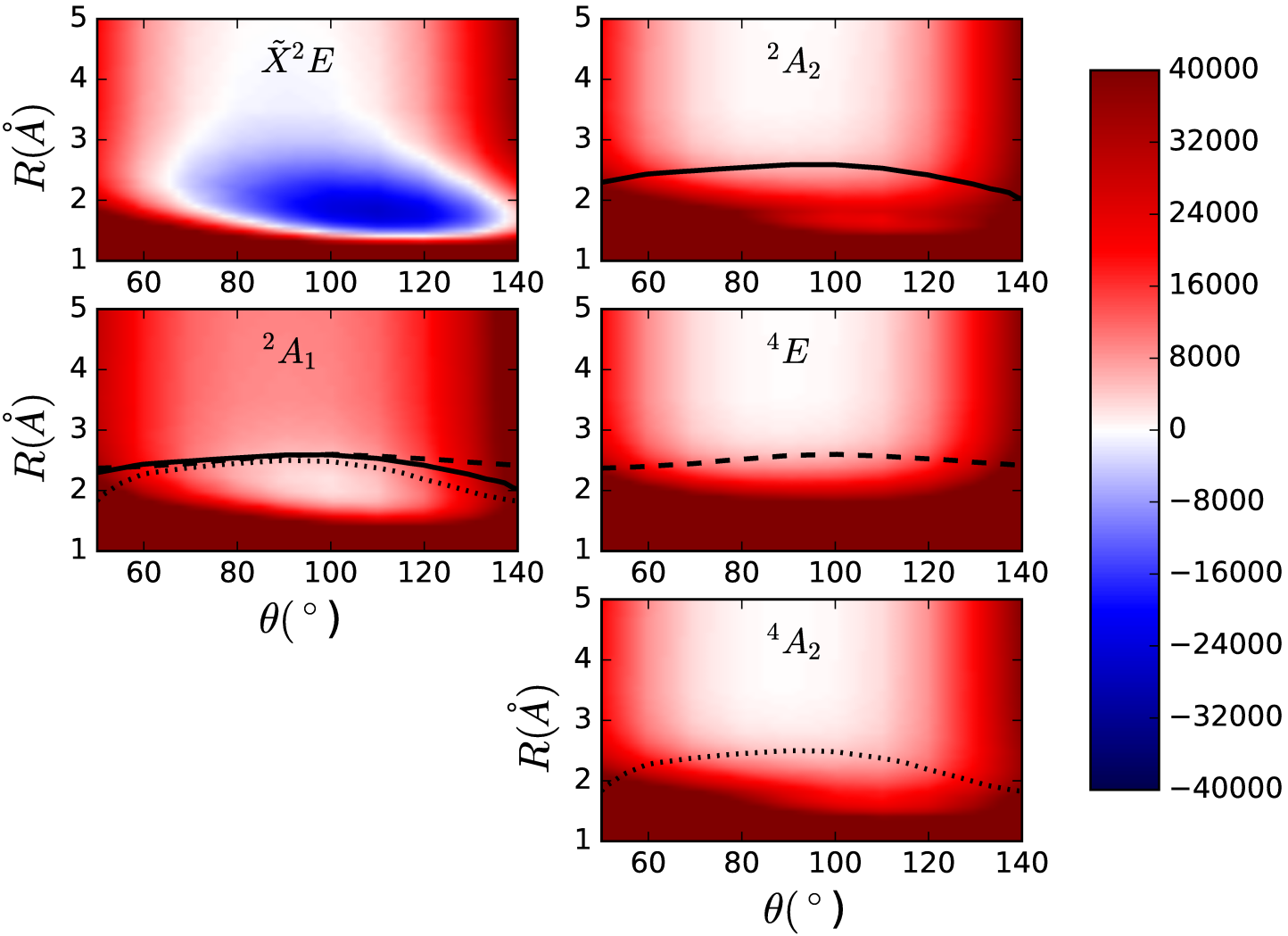
$\tilde{X}^2E$
$^2A_2$
$^2A_1$
$^4E$
$^4A_2$
$R(\mathring{A})$
$\theta(^\circ)$
1
2
3
4
5
60
80
100
120
140
40000
32000
24000
16000
8000
0
−8000
−16000
−24000
−32000
−40000

Fig. 9

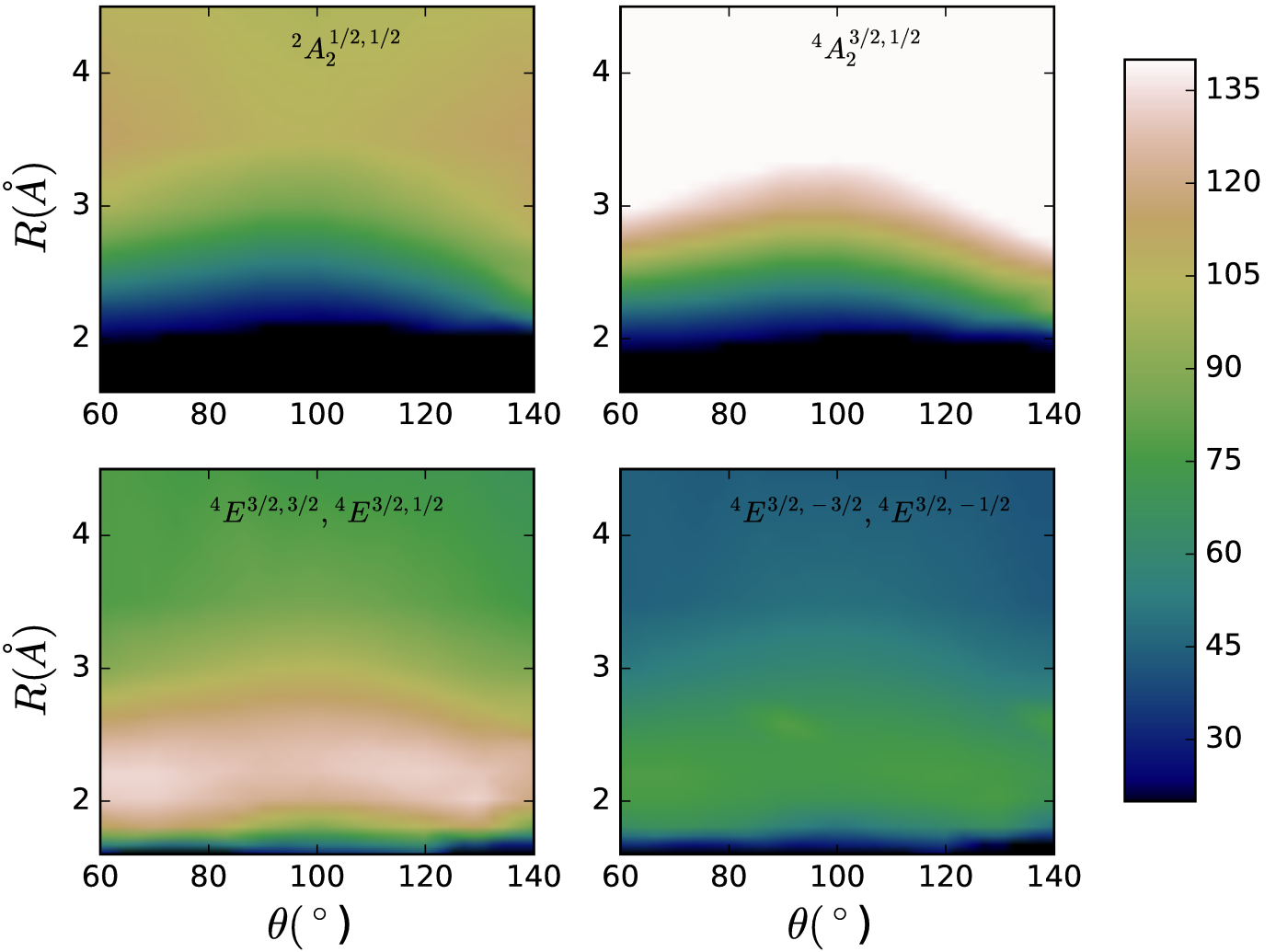
$^2A_2^{1/2,1/2}$
$^4A_2^{3/2,1/2}$
$^4E^{3/2,3/2}, ^4E^{3/2,1/2}$
$^4E^{3/2,-3/2}, ^4E^{3/2,-1/2}$
$R(\mathring{A})$
$\theta(^\circ)$
2
3
4
60
80
100
120
140
135
120
105
90
75
60
45
30